

A Systematic Study of Projection Biases in Weak Lensing Analysis

P.R.V. Chintalapati*

*Northern Illinois University and
Fermi National Accelerator Laboratory, P.O. Box 500, Batavia, IL 60510, USA.*

G. Gutierrez† and M.H.L.S. Wang‡

Fermi National Accelerator Laboratory, P.O. Box 500, Batavia, IL 60510, USA.

(Dated: May 17, 2022)

Using publicly available code and data, we present a systematic study of projection biases in the weak lensing analysis of the first year of data from the Dark Energy Survey (DES) experiment. In the analysis we used a Λ CDM model and three two-point correlation functions. We show that these biases are a consequence of projecting, or marginalizing, over parameters like h_0 , Ω_b , n_s and Ω_ν that are both poorly constrained and correlated with the parameters of interest like Ω_m , σ_8 and S_8 . Covering the relevant parameter space we show that the projection biases are a function of where the true values of the poorly constrained parameters lie with respect to the parameter priors. For example, biases can exceed the 1.5σ level if the true values of h and n_s are close to the top of the prior's range and the true values of Ω_b and Ω_ν are close to the bottom of the range of their priors. We also show that in some cases the 1D confidence intervals can be over-specified by as much as 30%. Finally we estimate these projection biases for the analysis of three and six years worth of DES data.

I. INTRODUCTION

Since its first statistically significant observations two decades ago [1–4], weak lensing has evolved to become a powerful tool in determining the values of important cosmological parameters. The recent results of the Dark Energy Survey (DES) experiment's first three years of data [5–9], the Hyper Suprime-Cam Subaru Strategic Program's (HSC) first year of data [10] and the Kilo Degree Survey's fourth data release (KiDS) [11–13], clearly show the power of weak lensing in measuring the normalization of the power spectrum σ_8 , the total relative matter density Ω_m , and their combination $S_8 = \sigma_8 \sqrt{\Omega_m/0.3}$. The already strong constraining power of weak lensing will rapidly increase with the analysis of the recently released shear catalog with three years of data from HSC [14], and the upcoming analysis of the full six years of data from DES. This constraining power will further increase with the upcoming “Stage IV” surveys like the Euclid Space Telescope [15] expected to launch in 2022, the Vera Rubin Observatory (LSST) [16] expected to start operating in mid-2020s, and the Nancy Roman Space Telescope [17] expected to launch also in the mid 2020s.

As the statistics and therefore the constraining power of these experiments continue to improve, it becomes increasingly important to understand any systematic and/or statistical biases present in the analyses. Different kinds of simulations have been used to test the performance of weak lensing analyses. For example, full N-body simulations have been used to assess biases in the shear measurement of galaxies or the errors in the

photometric measurements, as well as checking if the approximations made in the analysis theory, like the calculation of the non-linear power spectrum or the treatment of intrinsic alignment, introduces systematic errors in the measurements (see for example reference [18] for DES and [19] for KiDS). Faster simulations have been used to check, for example, the stability of the results to different aspects of the theory, or to validate covariance matrix models, or to study the effects of patchy sky coverage (see for example reference [20] for KiDS and [21] for DES). What all these simulations have in common is that they generally use one fixed set of parameters to generate the simulations.

In this paper we will be addressing the simpler question of how biases change, as we move through the parameter space, when having a perfect theory and when all measurement errors have been eliminated. One can answer this question by, 1) calculating a “synthetic data vector” using the analysis theory to generate the two-point correlation functions used in the analysis, 2) fluctuating this synthetic data vector using the data covariance matrix, 3) using this fluctuated synthetic data vector as input to the weak lensing analysis, and 4) repeating steps 2 and 3 a large number of times while checking at every iteration the measurements with the theory values. This clearly eliminates all questions about the validity of the theory and the existence of measurement errors. We will refer to every iteration as an “experiment” and to the entire process as “doing ensemble tests”.

Ensemble tests have the advantage of uncovering biases both in the shift and confidence intervals of the posterior distributions, but they are very CPU intensive due to the hundreds of jobs that need to be run in order to determine biases with enough statistical significance [22]. We will show that just running the synthetic data vector (no fluctuations, just “one experiment”) gives biases

* raj.ch90@gmail.com

† gaston@fnal.gov

‡ mwang@fnal.gov

in the shifts of the posteriors that are consistent with the ensemble tests. Therefore, in this publication, we performed studies with ensemble tests for only five different combinations of cosmological parameters, or five fiducial cosmologies, and then used synthetic data vectors to explore the rest of the parameter space. Synthetic data vectors have been used, for example, to study biases in the recently released DES weak lensing analysis [23]. In this reference only one fiducial cosmology was used, while in this paper we will cover all the relevant parameter space and show that, 1) the “projection biases” are a consequence of projecting, or marginalizing, the posterior distributions over parameters that are correlated with the parameters of interest and not well constrained, and 2) show that these biases are a function of where the true value of these poorly constrained parameters lie with respect to their prior intervals.

To perform the systematic study of projection biases presented in this paper, we used the publicly available code and data of the DES weak lensing analysis from their first year of data [24]. We restricted ourselves to using a Λ CDM cosmology and the so called 3x2pt analysis, which uses all three two-point correlation functions, termed galaxy clustering, galaxy-galaxy lensing, and cosmic shear. The bias studies of cosmic shear only (1x2pt), the combination of galaxy clustering and galaxy-galaxy lensing (2x2pt) and the effect of using a w CDM cosmology will be presented in a future paper.

In Section II, we summarize the model used in the analysis and give details of the public code that we used in our studies. In Section III, we describe a simple but very instructive example about how the projection biases arise when projecting over parameters that are not well constrained, and show our main results on the biases in the position and confidence intervals of the posterior distributions. In Section IV, we make a simple extrapolation to predict the projection bias behaviour with larger statistics, by dividing the data covariance matrix by factors corresponding to a DES analysis of three and six years worth of data.

Weak lensing provides tight constraints mostly on Ω_m , σ_8 , and S_8 , so most of the plots and projection biases shown in this paper will concentrate on those three parameters.

II. THE DES Y1 3x2pt WL ANALYSIS

For the projection bias studies presented in this paper, we will use the code that was developed by the DES collaboration to analyze the weak lensing (WL) data collected during the first year of observing (Y1) [24]. That code and the data are publicly available in CosmoSIS [25, 26]. Furthermore, we will concentrate on studying the projection biases in the case in which Λ CDM is the fiducial cosmology, and the cosmological parameters are extracted by fitting to all three two-point correlation functions: 1) Galaxy clustering, which correlates

the galaxy number densities along two different lines of sight (LOS), 2) Galaxy-galaxy lensing, that correlates the galaxy number density along a LOS with the galaxy shear along another LOS, and 3) Cosmic shear, which correlates galaxy shears along two different LOS. In all cases, the two-point correlations are given as a function of the angle θ separating the two LOS, and in bins of redshift along the LOS. In Subsection II A, we will give a short description of how the two-point correlations are calculated. In Subsection II B, we will describe the code that was used and how we selected the “true” or nominal values of the parameters for our studies.

A. The Model

In the weak lensing analysis of the data collected during the first year of running, DES used flat sky and Limber approximations to calculate two-point correlation functions. In this section, we will give a brief account of how the two-point correlation functions were calculated with the main purpose of making clear how the parameters listed in Table I enter in the analysis.

The main inputs to the calculation of the two-point correlation functions are the number density of galaxies in redshift bins and the power spectrum as a function of wavenumber k and time, or redshift. The measured galaxy number densities are given by

$$n_{g/\kappa}^i(\chi) = \hat{n}_{g/\kappa}^i(z) \frac{dz}{d\chi} \quad (1)$$

where χ is the comoving distance along the line of sight, z is the redshift, $\hat{n}_g^i(z)$ is the normalized galaxy number density for the i -th redshift bin, and $\hat{n}_\kappa^i(z)$ is the number density for galaxies that have a shear measurement. Throughout the paper, the relation between comoving distance and redshift $z = z(\chi)$ is calculated with the fiducial cosmology (Λ CDM in our case). In the DES analysis, the $\hat{n}_g^i(z)$ are referred to as the lens distributions and are given in five redshift bins, and the $\hat{n}_\kappa^i(z)$ are known as the source distributions and are given in four redshift bins. The uncertainties in the redshift measurements, for both the lens and source galaxies, are included in the analysis by shifting the original measured distribution $\hat{n}_{PZ}^i(z)$ as

$$\hat{n}^i(z) = \hat{n}_{PZ}^i(z - \Delta z^i) \quad (2)$$

where the nuisance parameters Δz_l^i and Δz_s^i for the lenses and sources are allowed to float in the analysis subject to the priors given in Table I. With the number density for galaxies with shear measurements, we can calculate the lensing efficiency as

$$\hat{q}^i(\chi) = \frac{3 H_0^2 \Omega_m}{2 c^2 a(\chi)} \int_\chi^{\chi_h} d\chi^s n_\kappa^i(\chi^s) \chi \left(1 - \frac{\chi}{\chi^s} \right) \quad (3)$$

where H_0 is the Hubble constant, c the speed of light, a the scale factor, and χ_h is the comoving distance at the

horizon. Note that, as expected, the lensing efficiency $\hat{q}^i(\chi)$ is zero for $\chi = 0$, or when the source is near the observer, it is small when χ coincides with the distance to the source galaxies, and it is maximum when χ is halfway between the observer and the sources.

The lensing efficiency has to be modified to account for the intrinsic alignment (IA) of galaxies [27, 28]. The “non-linear linear alignment” (NLA) model [29] was used in the DES Y1 WL analyses for the IA corrections, and Eq. 3 was modified as [21, 30]

$$q^i(\chi) = \hat{q}^i(\chi) - A_{IA} \left(\frac{1+z}{1+z_0} \right)^{\eta_{IA}} \frac{0.0134 \Omega_m}{D(\chi)} n_\kappa^i(\chi) \quad (4)$$

where $z_0 = 0.62$ and $D(\chi)$ is the linear growth factor. The nominal values and priors for the nuisance parameters, A_{IA} and η_{IA} , are given in Table I.

TABLE I. Table showing the parameters that were used in the DES Year 1 3x2pt WL analysis [24], together with their nominal values, range and priors. “Flat” denotes a prior that is flat within the given range and “Gauss(μ, σ)” specifies a gaussian prior with mean μ and variance σ^2 . The nominal values labeled as “varied” indicate the cases in which these parameters adopt different values during the projection bias studies in this paper (see Table III).

Parameter	Nominal	Range	Prior
Ω_m	0.267	(0.10, 0.90)	Flat
$A_s \times 10^9$	2.870	(0.50, 5.00)	Flat
n_s	varied	(0.87, 1.07)	Flat
Ω_b	varied	(0.03, 0.07)	Flat
h	varied	(0.55, 0.91)	Flat
$\Omega_\nu h^2 \times 10^3$	varied	(0.50, 10.0)	Flat
w	-1	fixed	
b_1	1.42	(0.8, 3.)	Flat
b_2	1.65	(0.8, 3.)	Flat
b_3	1.60	(0.8, 3.)	Flat
b_4	1.92	(0.8, 3.)	Flat
b_5	2.00	(0.8, 3.)	Flat
A_{IA}	0.44	(-5.0, 5.0)	Flat
η_{IA}	-0.7	(-5.0, 5.0)	Flat
$\Delta z_l^1 \times 10^2$	0.8	(-5.0, 5.0)	Gauss(0.8, 0.7)
$\Delta z_l^2 \times 10^2$	-0.5	(-5.0, 5.0)	Gauss(-0.5, 0.7)
$\Delta z_l^3 \times 10^2$	0.6	(-5.0, 5.0)	Gauss(0.6, 0.6)
$\Delta z_l^4 \times 10^2$	0.0	(-5.0, 5.0)	Gauss(0.0, 1.0)
$\Delta z_l^5 \times 10^2$	0.0	(-5.0, 5.0)	Gauss(0.0, 1.0)
$\Delta z_s^1 \times 10^2$	-0.1	(-10., 10.)	Gauss(-0.1, 1.6)
$\Delta z_s^2 \times 10^2$	-1.9	(-10., 10.)	Gauss(-1.9, 1.3)
$\Delta z_s^3 \times 10^2$	0.9	(-10., 10.)	Gauss(0.9, 1.1)
$\Delta z_s^4 \times 10^2$	-1.8	(-10., 10.)	Gauss(-1.8, 2.2)
$m^{i(=1,4)} \times 10^2$	1.2	(-10., 10.)	Gauss(1.2, 2.3)

In this paper, we use CAMB [31] to calculate the linear power spectrum, and then use this linear power spectrum as input to Halofit [32–34] to calculate the nonlinear power spectrum $\tilde{P}(k, z)$ in bins of (k, z) . The calculation of the power spectrum uses the seven cosmological parameters listed in the first part of Table I. The two-point correlation functions are calculated along two different

LOS separated by an angle θ . In the Limber approximation, only the modes in the power spectrum perpendicular to the LOS contribute to the two-point correlations. When oscillations along the LOS are very long, then $k_{\parallel} \ll k_{\perp}$ and $k \approx k_{\perp}$; and when the oscillations are very short, they average the contribution to the integrals to zero. Then, in the Limber approximation, only $\tilde{P}(k_{\perp}, z)$ enters in the calculation of the two-point correlations with $k_{\perp} = (l + 1/2)/\chi$. In the flat sky approximation, the two-point correlations are calculated with a double integration involving Bessel functions $J_n(x)$, and the three two-point (3x2pt) correlation functions used in the WL analysis fits are:

$$\hat{w}^i(\theta) = \int \frac{dl}{2\pi} l J_0(l\theta) \int \frac{d\chi}{\chi^2} [n_g^i(\chi)]^2 \tilde{P}(k_{\perp}, z) \quad (5)$$

for the galaxy clustering two-point correlation function,

$$\hat{\gamma}_t^{ij}(\theta) = \int \frac{dl}{2\pi} l J_2(l\theta) \int \frac{d\chi}{\chi^2} n_g^i(\chi) q^j(\chi) \tilde{P}(k_{\perp}, z) \quad (6)$$

for the galaxy-galaxy lensing two-point correlation function, and

$$\hat{\xi}_{+/-}^{ij}(\theta) = \int \frac{dl}{2\pi} l J_{0/4}(l\theta) \int \frac{d\chi}{\chi^2} q^i(\chi) q^j(\chi) \tilde{P}(k_{\perp}, z) \quad (7)$$

for the cosmic shear two-point correlation function. In all cases, the indices i, j label the redshift bins of the lens and source $\hat{n}(z)$ distributions. The two-point correlations calculated above need two corrections. One is due to the fact that the galaxy number density $n_g^i(\chi)$ only accounts for the visible matter, while light is lensed by all the matter it encounters in its path. A galaxy bias parameter b_i is added to each lens redshift bin to account for that effect. DES also accounted for small biases in the galaxy shear measurements by adding a nuisance parameter m^i , resulting in the final forms of the two-point correlation functions given by

$$w^i(\theta) = b_i^2 \hat{w}^i(\theta) \quad (8)$$

$$\gamma_t^{ij}(\theta) = b_i (1 + m^j) \hat{\gamma}_t^{ij}(\theta) \quad (9)$$

$$\xi_{+/-}^{ij}(\theta) = (1 + m^i) (1 + m^j) \hat{\xi}_{+/-}^{ij}(\theta) \quad (10)$$

The nominal values, intervals, and priors for the galaxy biases b_i and the shear nuisance parameters m^i are given in Table I.

B. DES Y1 WL Analysis Public Data and Code

As mentioned earlier, the data and the code that was used in the weak lensing analysis of the data collected by DES in the first year of running (DES Y1 WL) are publicly available in CosmoSIS [25, 26]. To avoid different versions of the CosmoSIS libraries that were used in the DES Y1 WL analysis, we used the version of CosmoSIS closest to that used in the publication describing the DES

Y1 WL analysis results [35]. As described below, some of the parameters in the CosmoSIS version of the DES analysis were changed to better reflect our understanding of how the analysis was done. This mostly applies to parameter values that are not well documented.

In the DES Y1 WL version stored in CosmoSIS the inner integrals in Equations 5 to 7 are calculated in the range $0.1 \leq l \leq 5 \times 10^5$ with 400 logarithmically spaced points. After checking that the differences in the analysis between using 200 or 400 points are small, we decided to reduce the number of points to 200. Using 400 points would have almost doubled the five months of computing time (using 1728 CPUs) required to do the studies presented in this paper. It is worth noting that the recently released DES results using three years of data used 100 points to calculate these integrals.

CosmoSIS uses the Multinest sampler [36] in the version of the DES Y1 WL analysis. Multinest searches and saves points in increasing values of the posterior and assigns a weight to each saved point. In the early iterations the weights are essentially zero because the points are far from the peak of the likelihood, and in late iteration the weights go to zero again because the phase space near the peak of the likelihood goes to zero. The number of iterations is controlled by the *tolerance* parameter and we changed its value from *tolerance* = 0.1 to *tolerance* $\leq 10^{-3}$ to make sure that the number of iteration would always be large enough such that the weights would go back to zero after they peaked.

As it is standard practice in weak lensing analyses, we processed the output of Multinest using Chainconsumer [37]. This program uses a Gaussian Kernel Density Estimator algorithm [38] to smooth the irregularities produced by the finite number of points provided by posterior samplers like Multinest. The width of the Gaussian Kernel is controlled by a parameter call KDE. A marginally low value of KDE=1.0 doesn't produce smooth 95% confidence edges in two dimensional posteriors and for wide posteriors some times it produces disconnected two dimensional contour, so we selected a value of KDE=1.5. The consequences of selecting this value are discussed at the end of Section III C.

The first four rows of Table II show the results of our analysis for different values of the KDE and the *tolerance* parameters. The final row shows the results of the DES Y1 WL analysis [24]. We can see that the differences only amount to a small fraction of the widths of the posteriors and are almost consistent with the inherent fluctuations of samplers like Multinest.

Figure 1 shows one and two dimensional posterior distributions for Ω_m , σ_8 and S_8 corresponding to row four of Table II. These plots should be compared with the "DES Y1 all" results in Figure 5 of reference [24]. We can see that the CosmoSIS version we will use in our studies reproduces the published results of the DES Y1 WL analysis very well.

For our studies we need to select a set of nominal or true values for the 26 parameters that enter in the anal-

TABLE II. The first four rows in this table show the results of our analysis of the DES Y1 weak lensing data. The last row shows the results of the published DES Y1 WL analysis [24]. We can see that the version of CosmoSIS we will use in our studies reproduces the DES published results very well.

Ω_m	S_8	σ_8	KDE	tol
$0.267^{+0.036}_{-0.021}$	$0.776^{+0.026}_{-0.022}$	$0.812^{+0.054}_{-0.060}$	1.0	0.1
$0.271^{+0.033}_{-0.027}$	$0.776^{+0.026}_{-0.024}$	$0.807^{+0.063}_{-0.057}$	1.5	0.1
$0.271^{+0.031}_{-0.025}$	$0.777^{+0.024}_{-0.022}$	$0.808^{+0.059}_{-0.052}$	1.0	10^{-3}
$0.272^{+0.032}_{-0.027}$	$0.777^{+0.026}_{-0.023}$	$0.810^{+0.059}_{-0.056}$	1.5	10^{-3}
$0.267^{+0.030}_{-0.017}$	$0.773^{+0.026}_{-0.020}$	$0.817^{+0.045}_{-0.056}$	DES Y1 WL	

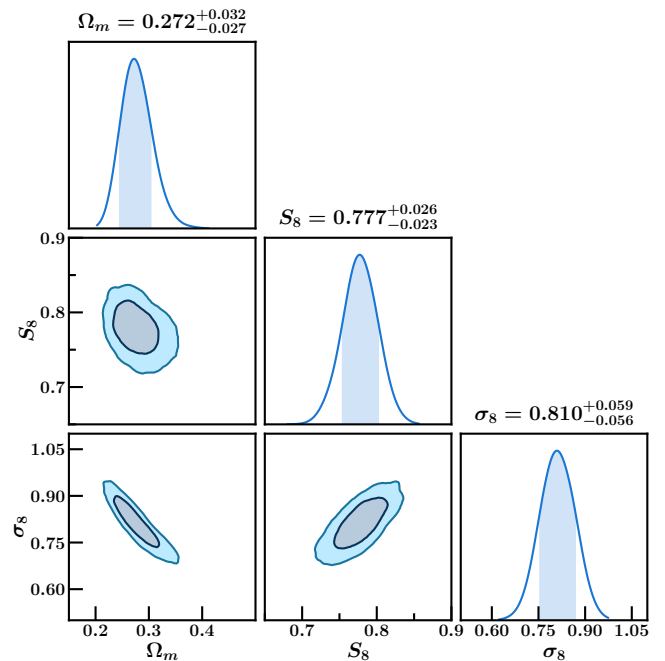


FIG. 1. This Figure shows the results of our analysis of the DES Y1 WL data using the DES Y1 data and programs publicly available in CosmoSIS. The plots correspond to row four of Table II.

ysis. The measured values of Ω_m , the biases b_1 to b_5 and the intrinsic alignment parameters A_{IA} and η_{IA} are given in the DES Y1 publication [24], so we used those values as the true or nominal values of the parameters. For the nuisance parameters Δz_l^1 to Δz_l^5 , Δz_s^1 to Δz_s^4 and m^1 to m^4 we used the peak of the priors as our true values. The measured $\hat{n}_{g/\kappa}(z)$ distributions given by default as input to CosmoSIS assume that $\Delta_{l/s}^i = 0$, so in order to avoid a mismatch between those distributions and the peak of the priors we shifted the $\hat{n}_{g/\kappa}$ distributions to match the

priors. After shifting the $\hat{n}_{g/\kappa}$ distributions we checked that the analysis of an input data vector calculated using the analysis theory and the true values of all the parameters gives a value of $\chi^2 = 0$ for the fit to the three two-point correlations functions and that the likelihood peak is lined up with the peak of the priors. This means that the peak of the overall posterior exactly coincides with the true values of all the parameters. Therefore any biases observed in the 1D, or 2D, posteriors are entirely due to projection effects.

TABLE III. List of nominal or true values used for the cosmological parameters h , Ω_b , n_s and $\Omega_\nu h^2$. The numbers in parenthesis indicate the parameter value as a percent of the parameter's prior range. All combinations of the values listed in the last three rows (3^4 combinations) were studied. The rest of the true values are given in Table I.

h	Ω_b	n_s	$\Omega_\nu h^2 \times 10^3$
0.692	0.0504	0.975	0.615
0.692	0.0504	0.975	4.5
0.692	0.0504	0.975	9.0
plus all 81 combinations of the following values			
0.64 (25)	0.04 (25)	0.92 (25)	0.615 (1.2)
0.73 (50)	0.05 (50)	0.97 (50)	4.5 (42.1)
0.82 (75)	0.06 (75)	1.02 (75)	9.0 (89.5)

For the true values of the cosmological parameters with wide prior distributions, h , Ω_b , n_s and $\Omega_\nu h^2$, we used the values listed in Table III. The values of h , Ω_b and n_s of the first three rows in the table correspond to our first determination of those values in the analysis of the DES data. As we will see in the following section, the projection biases are a function of where the true values sit in relation to the parameter range. Therefore the previous values were paired with three different values of $\Omega_\nu h^2$, 0.615×10^{-3} which corresponds to the minimum allowed by neutrino oscillation experiments, and 4.5×10^{-3} and 9.0×10^{-3} which sit close to the middle and the upper end of the $\Omega_\nu h^2$ prior range. For h , Ω_b and n_s we also selected true values of the parameters at 25%, 50% and 75% of their prior's range and paired all their combinations with the $\Omega_\nu h^2$ values described above, giving the $3^4 = 81$ combinations listed in the last three rows of Table III. These total of 84 different true values uniformly cover the volume of the four cosmological parameters with wide priors.

The posterior distribution for the intrinsic alignment parameter η_{IA} is also very wide but its correlations with Ω_m , σ_8 and S_8 are very weak so in our studies we didn't change the true value of this parameter. Also there are parameters that are strongly correlated, like Ω_m and the galaxy biases b_1 to b_5 , but all their posteriors fit comfortably within their prior ranges so we didn't change the true values of these parameters either.

III. PROJECTION BIASES

In this section we will describe the results of our projection bias study for the DES Y1 Weak Lensing analysis. To illustrate the origin of the projection biases, in Subsection III A we will describe a simple two dimensional example that contains all the characteristics observed in the real study. This simple example has several advantages, it is conceptually simple to visualize, it can be easily solved and it runs very fast so accumulating large statistics to reduce fluctuations is not a problem. In Subsection III B we will describe the effect that the projection biases have in the most likely value of the parameters (the peak of the posteriors) and in Subsection III C we will describe how the projection biases affect the 68.27% confidence intervals. For clarity, the projection bias effects in the most likely values and in the confidence intervals will be presented separately, but they are clearly related. A shift of the posterior relative to the true value of the parameter will also reduce the number of times the true value falls inside the confidence interval.

A. A Simple Example of Projection Biases

Given a data set \mathbf{d} and, for a given theory (in our case always Λ CDM), a set of parameters θ , Bayes theorem states that

$$P(\theta|\mathbf{d}) = \frac{P(\mathbf{d}|\theta)P(\theta)}{P(\mathbf{d})} \quad (11)$$

In the DES Y1 WL analysis the vector \mathbf{d} is comprised of the 457 points that are used in the fit of the galaxy clustering, galaxy-galaxy lensing and cosmic shear two-point correlation functions. $P(\mathbf{d}|\theta)$ is the probability density function of obtaining the data set \mathbf{d} given the parameters θ and, for WL analysis, this probability is given by the likelihood \mathcal{L} obtained fitting the data points \mathbf{d} to a theory prediction calculated using the parameters θ . The prior $P(\theta)$ includes knowledge external to the fit and, for all the θ parameters used in the DES Y1 WL analysis, these priors are listed in Table I. The Bayesian evidence $\mathcal{Z} = P(\mathbf{d})$ is given by

$$\mathcal{Z} = \int P(\mathbf{d}|\theta) P(\theta) d\theta \quad (12)$$

One and two dimensional projections of the posterior $P(\theta|\mathbf{d})$, for some of the cosmological parameters involved in WL analysis, are shown in Figure 3. In the two dimensional projections plots, e.g. h vs. Ω_m , we can see clear correlations between parameters whose likelihoods fit well inside the interval, like Ω_m , σ_8 and S_8 (the last two are not shown in the plots), and parameters for which the likelihood is wider than the specified interval, like h , Ω_b , n_s and $\Omega_\nu h^2$. Projections, or marginalization, over correlated parameters can introduce biases. This is especially the case when marginalizing over parameters with

likelihoods wider than the range of their priors and making measurements of parameters with likelihoods narrower than their priors. In this section we will illustrate how this works with a simple two dimensional example in which the likelihood for the first and second variable is respectively narrower and wider than their respective priors. This exemplifies, for example, the 2D-plots of h vs. Ω_m , or Ω_b vs. Ω_m shown in Figure 3. As we will see this simple example has all the same features we will encounter in Sections III B and III C when studying the projections biases in the DES Y1 WL analysis.

In our two dimensional example we will write Eq. 11 as

$$P(x, y) = \frac{1}{Z} \mathcal{L}(x, y) \pi(y) \quad (13)$$

where the posterior $P(x, y)$, the likelihood $\mathcal{L}(x, y)$ and the prior $\pi(y)$ are each normalized to one, the prior is given by

$$\pi(y) = \begin{cases} 1/(b-a) & \text{if } a \leq y \leq b \\ 0 & \text{otherwise} \end{cases} \quad (14)$$

and, writing $\mathbf{x} = (x, y)$ and $\bar{\mathbf{x}} = (\bar{x}, \bar{y})$, our likelihood will be given by the two dimensional Gaussian

$$\mathcal{L}(\mathbf{x}|\bar{\mathbf{x}}) = \frac{1}{2\pi\sqrt{\sigma_1\sigma_2}} e^{-\frac{1}{2}\chi^2}, \text{ with } \chi^2 = \mathbf{u}^T C^{-1} \mathbf{u} \quad (15)$$

The parameters σ_1 , σ_2 and α are the semi-axis and rotation angle of the ellipse with $\chi^2 = 1$, $\mathbf{u} = (u, v) = [(x - \bar{x})/\sigma_x, (y - \bar{y})/\sigma_y]$, with $\sigma_x = [(\cos\alpha/\sigma_1)^2 + (\sin\alpha/\sigma_2)^2]^{-1/2}$ and σ_y is obtained transposing $\sigma_1 \leftrightarrow \sigma_2$ in σ_x . The inverse of the correlation matrix, C^{-1} , is given by

$$C^{-1} = \begin{bmatrix} 1 & r \\ r & 1 \end{bmatrix} \quad (16)$$

where $r = \sigma_x \sigma_y \sin \alpha \cos \alpha (1/\sigma_1^2 - 1/\sigma_2^2)$.

For our studies we selected $\alpha = -20$ degrees, $\sigma_1 = 1$ and $\sigma_2 = 5$ which gives posteriors similar to the ones observed in the two dimensional plots involving Ω_m and displayed in Figure 3. Projection biases depend on the relative position of the "True" values with respect to the prior range, so to illustrate this we selected three symmetric prior intervals and three different true values in each of these intervals. The selected prior intervals are: $(a, b) = (-y_L, y_L)$, with $y_L = 7, 4$ and 2 , and the selected "True" value of the parameters are: $\mathbf{x}_T = (x_T, y_T) = (0, -R y_L)$, with $R = 0.9, 0.5$ and 0 . We didn't consider values of R greater than one because we assumed that the true value of the parameters are always inside the specified prior range. Also, we only considered true negative values of y because the corresponding positive values give exactly the same results but with all the distributions reflected around $x = 0$.

The top row of plots in Figure 2 show the $\chi^2 = 1$ contours of the $\mathcal{L}(\mathbf{x}|\mathbf{x}_T)$ likelihood for different values of

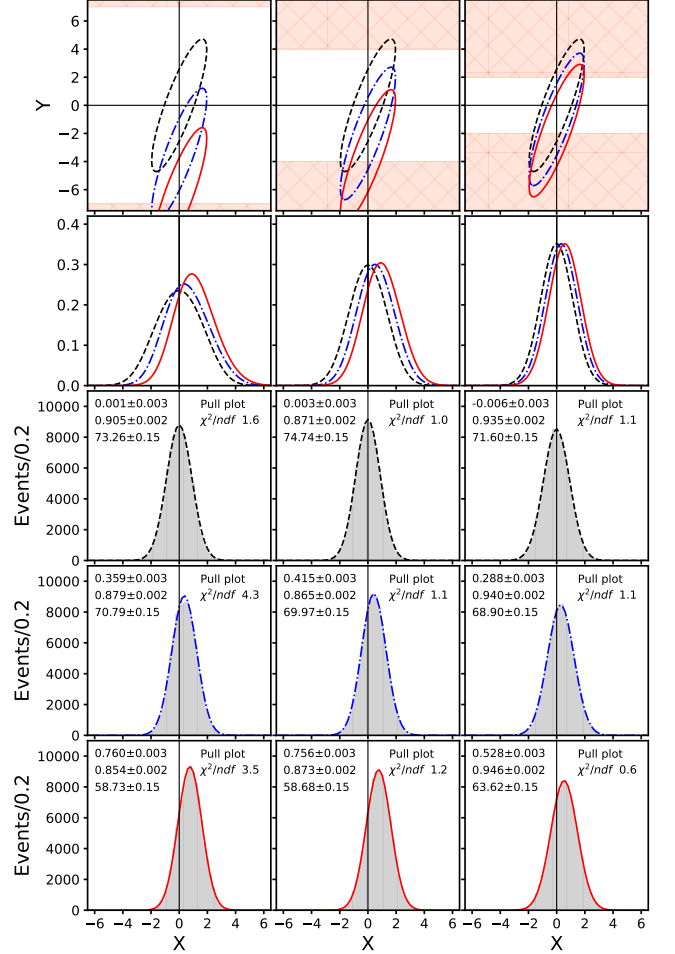


FIG. 2. Each column in this figure corresponds to different values of the prior $\pi(y)$, with $(a, b) = (-y_L, y_L)$ and $y_L = 7, 4$ and 2 for the left, center and middle columns. The shaded area in the top row plots shows the region excluded by the priors. The different line types correspond to different parameter's true values, $\mathbf{x}_T = (0, -R y_L)$ with $R = 0, 0.5$ and 0.9 for the dashed, dash-dotted and solid lines. The top row plots show the $\chi^2 = 1$ contours of $\mathcal{L}(\mathbf{x}|\mathbf{x}_T)$ for the values of \mathbf{x}_T given above. The second row shows the 1D-posteriors when marginalized over y , which is to say the projections of the corresponding likelihoods times the priors given in the first row plots. Rows three to five show the pull given histograms, and Gaussian fits, for different true values, with $R = 0, 0.5$ and 0.9 for rows three, four and five respectively. See text for more details.

R . For all plots in Figure 2, the dashed (black), dash-dotted (blue) and solid (red) lines correspond to $R = 0, 0.5$ and 0.9 . The shaded areas in the top row plots indicate the values of y excluded by the priors. Each column in Figure 2 corresponds to different values of the prior, with $y_L = 7, 4$ and 2 for the left, center and middle columns.

The marginalization of the posterior over the y variable

can be calculated exactly as

$$P(x) = \int_a^b dy \mathcal{L}(\mathbf{x}|\bar{\mathbf{x}}) \quad (17)$$

$$= \sqrt{\frac{1-r^2}{8\pi\sigma_x^2}} e^{-\frac{1}{2}u^2(1-r^2)} [\text{erf}(t_b) - \text{erf}(t_a)] \quad (18)$$

where $t_a = [(a-\bar{y})/\sigma_y + ru]/\sqrt{2}$, t_b is calculated replacing a by b in t_a , and $\text{erf}(x)$ is the error function. The results of this marginalization for $\bar{\mathbf{x}} = \mathbf{x}_T$ is shown in the second row of plots in Figure 2. Each dashed, dash-dotted or solid line curve corresponds to the marginalization of the dashed, dash-dotted or solid line two dimensional posteriors shown in the first row plots. Given that the "True" value is at $x = 0$, we can see how the marginalization, or projection, produces biases in the projected or marginalized posteriors, and how this projection biases depend on how the prior is selected relative to the unknown true value of the parameters being marginalized. In the real case these plots would correspond to the one dimensional posteriors of, for example, Ω_m , σ_8 or S_8 when marginalized over all other variables. From the two top row plots in Figure 2 we can also see that for an ellipse with a negative or clockwise rotation the projection bias will go from maximum positive to minimum negative values when the true value of the wide posterior parameters goes from the lower to the upper edge of the interval. The opposite is true if the ellipse has a positive rotation, that is, the bias will go from minimum to maximum values when the true value goes from the lower to the upper edge of the interval.

Biases in the projected distribution would not be a problem if the interval corresponding to the 68.27% area of the posterior included the true value of the parameter 68.27% of the time. In order to test if this is true we need to simulate doing the same experiment many times and count how often the true value falls inside the 68.27% interval. We will call this process doing ensemble tests and refer to each simulated experiment as a pseudo-experiment. If we imagine performing the DES WL experiment many times, subject only to statistical fluctuations, in each new experiment we will get a new value of the data set \mathbf{d} which when fitted will lead to a new likelihood and the extraction of new parameter values $\bar{\mathbf{x}}$. If the covariance matrix used in the fit was calculated correctly then the values of $\bar{\mathbf{x}}$ will follow a distribution given by $\mathcal{L}(\bar{\mathbf{x}}|\mathbf{x}_T)$ (see Equation 15 for the two dimensional case), where nature has selected and fixed the value of \mathbf{x}_T .

Then our ensemble test proceeds according to the following steps. After selecting the true parameter values \mathbf{x}_T , each pseudo-experiment is generated as: 1) calculate a random value of $\bar{\mathbf{x}}$ using the distribution $\mathcal{L}(\bar{\mathbf{x}}|\mathbf{x}_T)$ given in Eq. 15 (notice the different arguments), 2) calculate the 1D-posterior $P(x)$ marginalizing $\mathcal{L}(\mathbf{x}|\bar{\mathbf{x}})$ using Eq. 18, 3) calculate the peak and the minimum interval containing the 68.27% area under $P(x)$, and 4) enter the values in the pull histogram as explained in the

next paragraph and check if the true value lies inside the calculated 68.27% minimum interval. Repeat, keeping \mathbf{x}_T fixed, until reaching the desired number of pseudo-experiments (one hundred thousand in our case). The minimum interval (A, B) containing a fixed value of the area under the posterior $P(x)$ is obtained with the condition $P(A) = P(B)$ (see Appendix A).

Each pseudo-experiment provides the peak of the posterior x_p , and two errors σ_- and σ_+ (both positive). Since in ensemble tests the true value x_T is known we can form the pull distribution as [39]:

$$\begin{cases} \text{pull} = (x_p - x_T)/\sigma_+ & , \text{ if } x_T > x_p \\ \text{pull} = (x_p - x_T)/\sigma_- & , \text{ if } x_T \leq x_p \end{cases} \quad (19)$$

For asymmetric errors the pull is defined as in the above equation because for $x_T > x_p$ we are comparing x_T with the positive part of the posterior distribution and when $x_T < x_p$ the comparison is with the negative part.

The pull plots are shown in rows three to five of Figure 2. Each pull row corresponds to different true values of the parameters $\mathbf{x}_T = (0, -R y_L)$, with $R = 0, 0.5$ and 0.9 for rows three, four and five. Each column corresponds to different values of the prior $(a, b) = (-y_L, y_L)$, with $y_L = 7, 4$ and 2 for the left, center and right columns. The pull histograms were fit to a Gaussian distribution, the mean and σ resulting from the fit, with its errors, are shown in the upper and center left legends in each plot. The lower left legend shows the probability that the 68.27% interval will include the true value of the parameter, the error was calculated assuming binomial statistics. The legend on the lower right shows the χ^2/ndf of the fit.

In the absence of biases the mean and rms of the fit to the pull plots should be zero and one, the probability should be 68.27% and the χ^2/ndf should be one. We verified that this is the case by selecting very large values of y_L . We also verified that the results are stable with respect to the parameters in the calculation, such as the number of bins used in the fit and the number of point and range in x that were used to calculate the minimum interval containing the 68.27% area of the posterior. As a double check we also verified that, within errors, there is agreement in the probability that the true value will fall inside the confidence interval obtained by counting or by calculating it using the mean and rms of the pulls. The χ^2 probabilities for the fits to the central and right column pull plots of Figure 2 are all larger than 20%. For the left column the χ^2 probabilities for the third, fourth and fifth rows are 1.2×10^{-2} , 1.2×10^{-16} and 1.3×10^{-11} respectively. This indicates that in seven out of nine cases the pulls are very Gaussian.

It is clear from the pull plots that even this simple example can exhibit large projection biases depending on the position of the true value relative to the prior range. We also see that in all cases the width of the pull is smaller than one, which means that the errors calculated from the posteriors are too large. Based on the rms of the pull plots, we calculate that the confidence intervals are between 5% and 15% larger than they should

be. In the next two sections we will observe the same biases in the DES Y1 Weak Lensing analysis. We will also see that these biases can be much larger than the ones encountered in this section, the reason for this is that in the real analysis there are four correlated wide distributions that contribute to the projection biases: h , Ω_b , n_s and $\Omega_\nu h^2$.

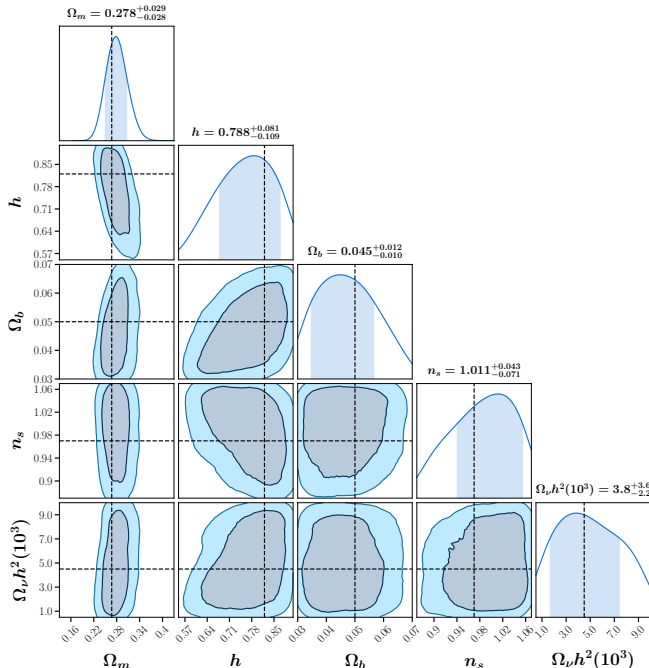


FIG. 3. Selected one and two dimensional posterior plots from the analysis of a synthetic data vector with true parameter values $h = 0.82$, $\Omega_b = 0.05$, $n_s = 0.97$ and $\Omega_\nu h^2 = 4.5 \times 10^{-3}$. The true or nominal values for the rest of the parameters are given in Table I.

B. Biases in the Posterior Peaks

To study statistical errors one imagines doing the same experiment a very large, or infinite, number of times. Then, in the absence of systematic errors the true value of the quantity we are trying to measure will lie inside the 68.27% confidence interval 68.27% of the time, and the proper average of the most likely value of that quantity will converge to the true value. In our case we simulated this process by fluctuating, using the covariance matrix, an exact calculation of the three two-point correlation functions and then used this fluctuated two-point correlations as input data to the analysis. This process, which as pointed out in Section I we are calling doing ensemble tests, is very CPU time intensive so for most of our studies we used a “synthetic data vector”. We will show that for studying biases in the position of the posterior distributions there is good agreement between the two methods.

A synthetic data vector is composed of three two-point correlation functions, as a function of the angles used in the analysis, calculated using the true or nominal values of the parameters listed in Table III and the formalism summarized in Section II A. This synthetic data vector is then used to replace the input data in the DES Y1 WL analysis leaving everything else unchanged, e.g. the $\hat{n}_{g/\kappa}(z)$ distributions, covariance matrix, priors, etc. In this case the theory used in the analysis matches exactly the theory that generated the input data which eliminates all systematic errors, for example, from measurement errors or coming from discrepancies between the analysis theory and the data. Furthermore, since the true parameter values are known, this procedure allows for the study of sources of biases in the analysis that are not related to systematic errors. In this section we will discuss the results of the analysis of the 84 synthetic data vectors generated with the true values listed in Table III. In the following section we will discuss the ensemble tests performed on a selection of five of the 84 synthetic data vectors.

Figure 3 shows results of the analysis of a synthetic data vector generated with true values $h = 0.82$, $\Omega_b = 0.05$, $n_s = 0.97$ and $\Omega_\nu h^2 = 4.5 \times 10^{-3}$, corresponding to fractions of the parameter range of 0.75, 0.5, 0.5 and 0.421. All the other true or nominal values of the parameters are listed in Table I. To understand the behaviour of projection biases it is worth paying attention to the correlations seen in Figure 3 between Ω_m , and the parameters with wide priors h , Ω_b , n_s and $\Omega_\nu h^2$. Going down the first column, we see that there is a positive, or counterclockwise, correlation with h , and then the correlation alternates sign for Ω_b , n_s and $\Omega_\nu h^2$. This pattern of correlations is typical and fairly independent of the true values of the parameters, except that they mostly reverse sign for σ_8 and S_8 .

In the example given in Section III A we saw that the projection bias becomes positive and maximum when there is a negative, or clockwise, correlation and the true value of the parameter with the wide prior is at the lower end of its range. For a positive, or counterclockwise, correlation the opposite is true, the projection bias is at its maximum positive value when the true value of the parameter with the wide distribution is at the upper end of its range. For more than one parameter with wide priors the contributions to the projection bias will add, then we should expect that the bias in Ω_m will have a maximum positive value when the true value of h is near the upper end of the range, and the true values of Ω_b , n_s and $\Omega_\nu h^2$ are respectively near the lower, upper and lower ends of their ranges. And this is exactly what we will observe. Also we would expect that the bias reaches its lowest, or negative, value when the above four parameters are at the opposite end of their ranges, and again this is what we will observe.

Figure 4 shows the Ω_m , σ_8 and S_8 posterior distributions for the five cases in which we have results for both the synthetic data vector analysis and ensemble tests.

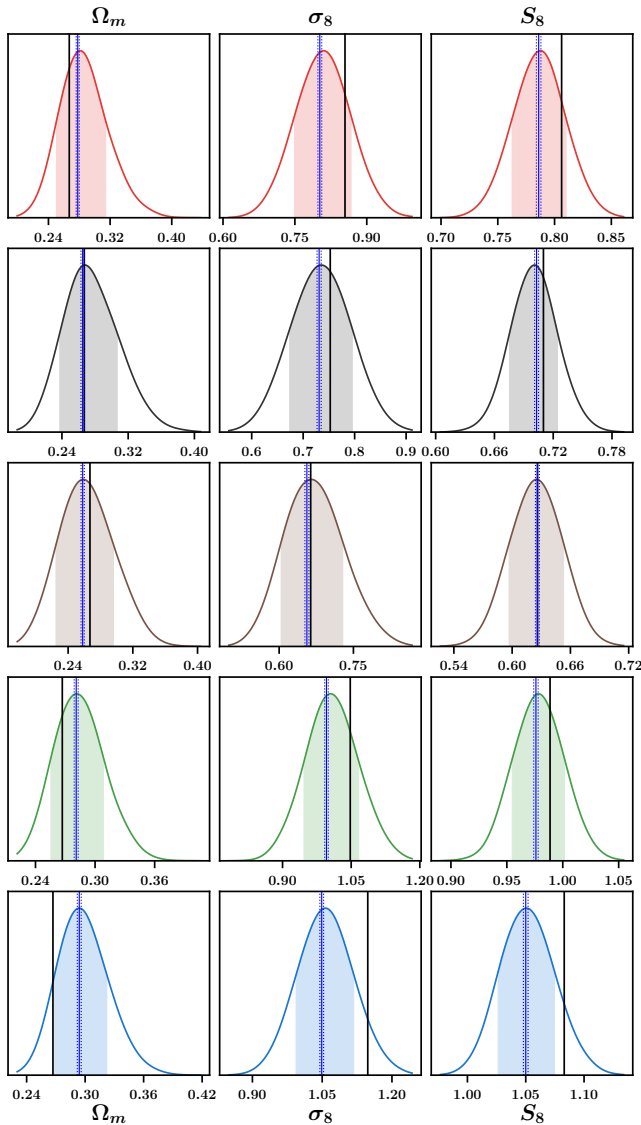


FIG. 4. Posterior distributions from the analysis of synthetic data vectors created with the true parameter values listed in Tables IV and I. The columns correspond to Ω_m , σ_8 and S_8 . The rows correspond to different values on the true parameters in the same vertical order they are listed in Table IV. The vertical solid lines correspond to the true value of the parameters, the vertical solid lines flanked by dotted lines correspond to the ensemble tests results.

The true values of h , Ω_b , n_s and $\Omega_\nu h^2$ used to make the plots in the figure are listed in Table IV, the rest of the true parameter values are given in Table I. The posteriors for the different cases in Figure 4 are given in the same vertical order as in Table IV. In all cases the distributions show the posterior for Ω_m , σ_8 and S_8 , and the shaded areas show the 68% area of the posteriors. The vertical solid lines show the true values of the corresponding parameters. We can clearly see that in most cases the true values and the peaks of the posteriors do not agree, which is the effect of the projection biases. We can also

TABLE IV. This table lists the nominal or true values of the cosmological parameters h , Ω_b , n_s and $\Omega_\nu h^2$ for which the projections biases were studied using both ensemble tests and analyzing a single synthetic data vector. The numbers in parenthesis indicate the parameter value as a percent of the parameter's prior range. The rest of the true values are given in Table I.

#	h	Ω_b	n_s	$\Omega_\nu h^2 \times 10^3$
1	0.692 (39)	0.0504 (51)	0.975 (53)	0.615 (1.2)
2	0.692 (39)	0.0504 (51)	0.975 (53)	4.5 (42.1)
3	0.692 (39)	0.0504 (51)	0.975 (53)	9.0 (89.5)
4	0.82 (75)	0.04 (25)	1.02 (75)	4.5 (42.1)
5	0.82 (75)	0.04 (25)	1.02 (75)	0.615 (1.2)

clearly see that these biases are a function of the true parameter values, with the biases being smaller when the true value of the parameters sit close to the middle of the prior interval. This is the same effect observed in the simple example studied in Section III A and exemplified in the second row plots of Figure 2 in that section.

The DES collaboration recently released the weak lensing results of their analysis of the first three years of data. The results from the fit to all three two-point correlation functions (3x2pt analysis) are given in Ref. [9]. The validation of the theoretical model used in the analysis is given in Ref. [23]. Figure 2 of this reference shows the projection biases for the true values of $h = 0.69$, $\Omega_b = 0.048$, $n_s = 0.97$ and $\Omega_\nu h^2 = 0.83 \times 10^{-3}$. As in our case, we can see that the biases for Ω_m and S_8 approach the 1σ level, but these biases were studied for only one set of true values of the parameters.

The vertical dashed lines, flanked by dotted lines, in Figure 4 show the results of the ensemble tests. The dashed (dotted) lines shows the most likely value (σ) obtained by multiplying the posteriors of all 220 runs in each ensemble test. We can see that the errors in the most likely value of the ensemble tests are very small and that there is very good agreement between the analysis using a synthetic data vector and the ensemble tests. This gives us confidence that we can discuss projection biases using mostly synthetic data vectors.

Figure 5 shows the bias in the peak of the posteriors for all 84 combinations of true values listed in Table III, five of these entries correspond to the peak of the posteriors shown in Figure 4. In all cases the posteriors were calculated using synthetic data vectors. The vertical scales show the peak of the posterior minus the true value divided by σ_+ , or σ_- , if the peak of the posterior is smaller, or greater, than the true value. The selection of which σ to use in the denominator is the same as in the definition of the pull in Eq. 19, when the peak of the posterior is smaller than the true value we are comparing the true value with the positive side of the posterior and when the peak of the posterior is larger than the true value the comparison is with the negative part of the posterior. The horizontal scale is a case number from 1 to 84. Each group of three points joined by a line correspond to three

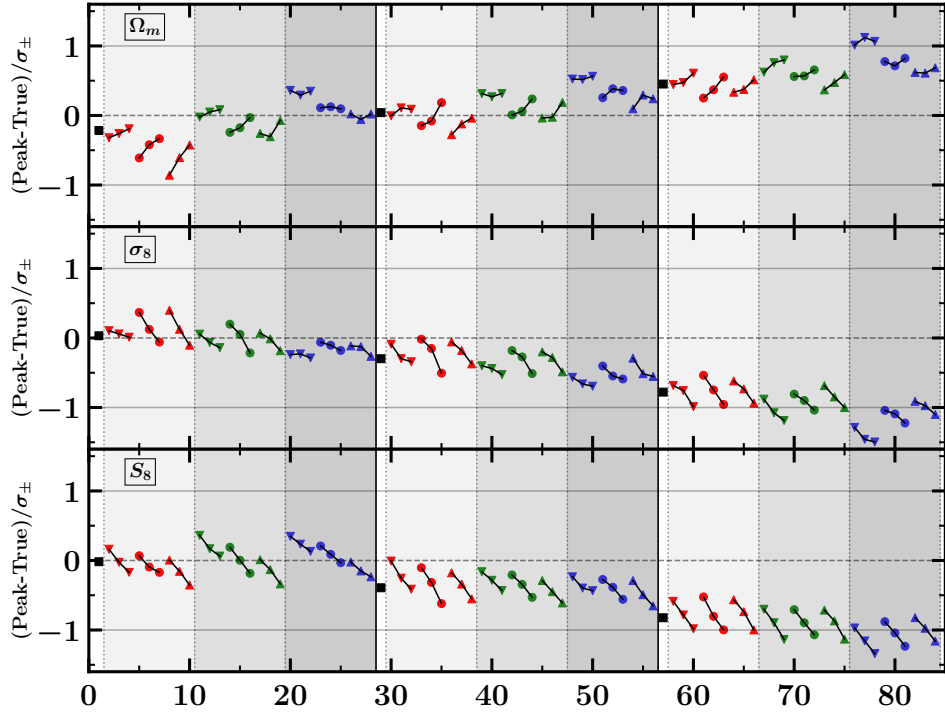


FIG. 5. Projection bias plots for the 84 combinations of parameter true values given in Tables I and III. The vertical scales show the peak of the posterior minus the true value divided by σ_+ (σ_-) if the peak of the posterior is smaller (greater) than the true value. The horizontal scale is a case number from 1 to 84. The groups of three points joined by a line correspond to different values of n_s . The downward triangles, circles and upward triangles correspond to different values of Ω_b . The shades of light, medium and darker grey correspond to different values of h . And the large left, middle and right groups of 27 points correspond to different values $\Omega_\nu h^2$. The values of n_s , Ω_b and h increase from left to right taking the values of 25%, 50% and 75% of the prior's range. $\Omega_\nu h^2$ decrease from left to right with values of 89.5%, 42.1% and 1.2% of the prior's range. The three solid squares correspond to the top three cases listed in Table III.

different values of n_s , and from left to right these values are 25%, 50% and 75% of the interval prior. The downward pointing triangles, the circles and the upward pointing triangles correspond to values of Ω_b of 25%, 50% and 75% of the prior's interval. The groups with background shades of light, medium and darker grey correspond to values of h of 25%, 50% and 75% of the prior's interval respectively. The large left, middle and right groups of 27 points correspond to values $\Omega_\nu h^2$ of 89.5%, 42.1% and 1.2% of the prior's interval respectively. Note that while the true values of n_s , Ω_b and h increase from left to right for $\Omega_\nu h^2$ the true values increase from right to left. Finally the three solid squares in between the larger groups of 27 points correspond to the top three cases listed in Table III.

As discussed earlier in this section, the overall pattern of the projection biases in Figure 5 can be understood with the correlations observed in the first column of Figure 3 and the simple example given in Section III A. In the top row plot of Figure 5 we see that the overall projection biases for Ω_m move towards increasing positive values with increasing values of n_s and h , and decreasing values of Ω_b and $\Omega_\nu h^2$. At the same time from the first column in Figure 3 we can see that the correlations with

Ω_m are positive (ellipse rotated counterclockwise) with n_s and h , and negative for Ω_b and $\Omega_\nu h^2$. In our simple example we saw that for negative (positive) correlations the projection bias moves towards more positive values when the value of the parameter decreases (increases). So the projection biases for Ω_m behave as expected. Since σ_8 is anti-correlated with Ω_m we would expect the opposite behaviour for σ_8 and this is what we observe comparing the first and second row plots in Figure 5. The behaviour of the projection bias for S_8 follows closely that of σ_8 except for the first light grey area where the very low values of the bias for Ω_m pull down the bias for S_8 .

Not surprisingly then, the largest projection biases in our 84 cases occurs when the true values of n_s , Ω_b , h and $\Omega_\nu h^2$ are at 75%, 25%, 75% and 1.2% of their respective ranges. The biases in this case are close to 1σ for Ω_m and to -1.5σ for σ_8 and S_8 . The projection biases would actually be larger if the true values would be pushed closer to the limits of their ranges, but we have assumed that the parameter ranges are selected conservatively and for n_s , Ω_b and h stayed within 25% of the edges of the parameter ranges. Of course for $\Omega_\nu h^2$ we selected true values very close to the lower range limit because a very low neutrino mass first eigenstate is always a real possibility.

As previously discussed the opposite values of the projection biases for Ω_m and σ_8 occur at the opposite true values of n_s , Ω_b , h and $\Omega_\nu h^2$ that is at 25%, 75%, 25% and 89.5% of their respective ranges. In this case the biases are about -1σ for Ω_m and 0.5σ for σ_8 . The highest positive bias for S_8 is also about 0.5σ but it is shifted due to the influence of the Ω_m biases on S_8 in the first light grey band.

C. Biases in the 68% Confidence Intervals

Five of the 84 cases discussed in the previous section were selected for ensemble tests. The true value of the parameters for these five cases are listed in Table IV. For each of these cases, 220 input data vectors were generated fluctuating the synthetic data vector using the covariance matrix. These new data vectors were then processed using the regular DES Y1 WL analysis. Results for Ω_m , σ_8 and S_8 of the 220 runs corresponding to the first row of true values in Table IV are shown in Figure 6. Each

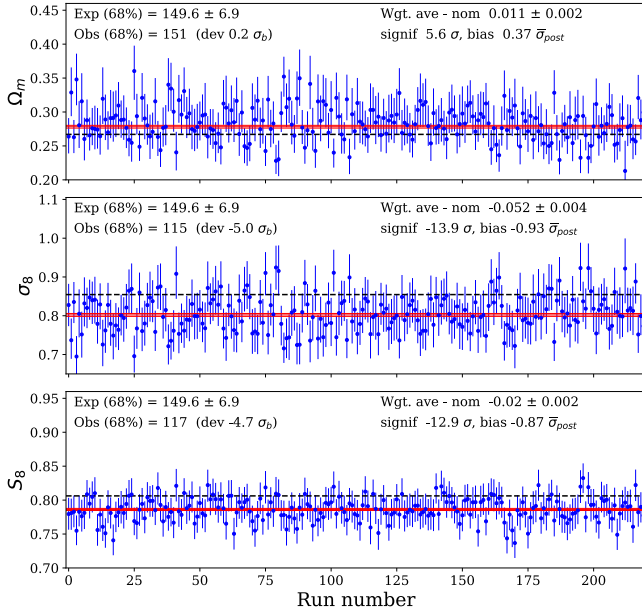


FIG. 6. Ensemble test results for Ω_m , σ_8 and S_8 . Each run is represented by a dot with error bars displaying the peak of the posterior and its errors. The horizontal axis displays the run number in the ensemble test. The dashed horizontal lines show the true values (see first row in Table IV) and the three horizontal solid lines show the weighted average and one sigma errors for the combination of all 220 runs.

dot with error bars in this figure represents the peak of the posterior and its errors for all 220 runs in this ensemble test. The dashed line represents the true value for the corresponding parameter. The weighted average (\bar{x}_W) and the error (σ) for the combined runs were obtained by multiplying the posteriors for all 220 runs. This weighted average minus the true or nominal value and the one sigma error are shown in the upper right side of the

plots. These values were also entered as the vertical line flanked by dotted lines in the upper row plots of Figure 4. The vertical line corresponds to \bar{x}_W and the flanking dotted lines to $\bar{x}_W \pm \sigma$. The vertical lines with flanked dotted lines in the other four rows of the same figure were calculated in a similar way from their corresponding ensemble tests. We can see that there is consistency between the projections biases obtained using a synthetic data vector and those obtained from ensemble tests. Also shown in the upper right side of the plots in Figure 6 are the significance defined as $(\bar{x}_W - \text{true})/\sigma$ and the bias defined as $(\bar{x}_W - \text{true})/\bar{\sigma}_{post}$, where $\bar{\sigma}_{post} = (\sigma_{post}^+ + \sigma_{post}^-)/2$ is the average of the positive and negative errors of the posterior. We can see that 220 runs are enough to determine the biases with a high degree of significance. The upper left side of each plot shows the expected (Exp) and observed (Obs) number of times the true value falls inside the 68.27% interval of the posterior. The error in the expected value (σ_b) was calculated using binomial statistics. The deviation is defined as the observed minus the expected number of events divided σ_b , $\text{dev} = (\text{Obs} - \text{Exp})/\sigma_b$. Given the biases in the posteriors it is not surprising that for σ_8 and S_8 the number of observed cases where the true value falls inside the posterior's 68.27% interval is substantially lower than expected with a high degree of significance.

The best way to visualize the projection biases in both the most likely values and the confidence interval of the posteriors is with pull plots. The pull is defined as in Equation 19. Figure 7 shows the pull plots for the five ensemble test cases outlined in Table IV. The vertical order in the pull plots is the same as in the table. For infinity statistical samples and in the absence of biases these plots will be Gaussian distributions with mean $\bar{x}_p = 0$ and sigma equals to $\sigma_p = 1$. The solid lines in the plots show the Gaussian fit to the histograms. The interval used in the fit extends to $\pm 3.0\sigma$ from the peak of the distributions. We checked that the fit results are stable with the selection of this interval and with the selection of the bin size. The top and center legends on the left side of each plot show the average (\bar{x}_p) and sigma (σ_p) of the Gaussian fits. From top to bottom the legends on the right show χ^2/ndf , the number of degrees of freedom (ndf) and the χ^2 probability for the fits. The probability that the true value will be inside the 68.27% confidence interval (P_{68}) is given by the lower value on the left legends. P_{68} was calculated by simply counting the number of times the true value was inside the 68.27% area of the posterior. We can see that overall the fits look very Gaussian, but there are large biases in both the mean and sigma of the fits. The values of σ_p range from 0.67 to 0.94 indicating that in all cases the posterior confidence intervals are too wide (the average width of the CI is $1/\sigma_p$). This is consistent with the pulls observed in our simple example in Section III A and in Figure 2. In many cases we can also see a substantial shift in the pull distribution to the point that even with very inflated confidence intervals the P_{68} probability can be as low as

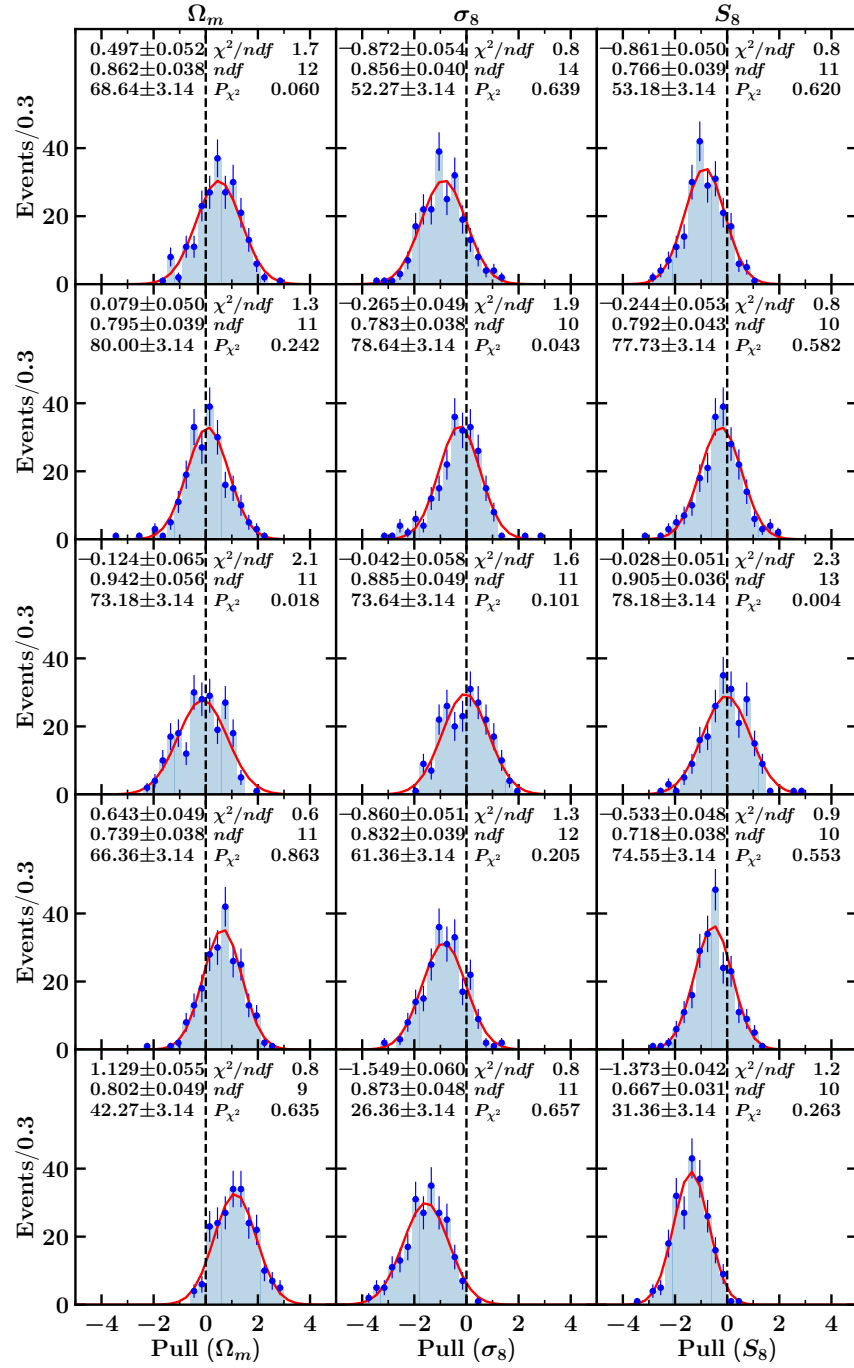


FIG. 7. Histograms of the pull values shown in Equation 19 for the five ensemble tests with the true values given in Table IV. The vertical order is the same as in the table, the points with error bars show the number of entries in each bin with their binomial errors. From top to bottom the left side legends show the mean (\bar{x}_p) and sigma (σ_p) of the Gaussian fit to the histogram and the probability (P_{68}) that the true value will lie inside the 68.27% confidence interval. The right legends show χ^2/ndf , the number of degrees of freedom (ndf) and the χ^2 probability of the Gaussian fits.

27%.

the expression (see Appendix B)

$$P_{68}(\text{pull}) = \frac{1}{2} \left\{ \text{erf} \left(\frac{1 - \bar{x}_p}{\sqrt{2} \sigma_p} \right) + \text{erf} \left(\frac{1 + \bar{x}_p}{\sqrt{2} \sigma_p} \right) \right\} \quad (20)$$

We can check the consistency of the pulls by calculating the P_{68} probability from the pull parameters using

and then comparing it with the P_{68} probability obtained

by counting. The P_{68} probability obtained by counting is shown in the first row in each of the Ω_m , σ_8 and S_8 groups in Table V. From left to right each column in the table corresponds to the top to bottom plots in Figure 7. The second row in each group corresponds to the P_{68} probabilities calculated from the pull parameters using Equation 20, and the third row is the difference between the two calculations divided by the error in the P_{68} probability obtained by counting. We can see that the two ways of obtaining P_{68} are completely consistent with each other.

TABLE V. Table of probabilities that the true value will fall inside the 68.27% interval. For each parameter the first row shows the values obtained by counting, the second row are the values calculated from the pull plots (see Equation 20) and the third row is the difference divided by the error in the probability obtained by counting.

	1	2	3	4	5
Ω_m	68.6 \pm 3.1	80.0 \pm 3.1	73.2 \pm 3.1	66.4 \pm 3.1	42.3 \pm 3.1
	67.9 \pm 2.1	78.9 \pm 2.2	70.7 \pm 2.9	67.2 \pm 2.5	43.2 \pm 2.6
	-0.2	-0.3	-0.8	0.3	0.3
σ_8	52.3 \pm 3.1	78.6 \pm 3.1	73.6 \pm 3.1	61.4 \pm 3.1	26.4 \pm 3.1
	54.5 \pm 2.3	77.3 \pm 2.2	74.1 \pm 2.6	55.4 \pm 2.3	26.3 \pm 2.4
	0.7	-0.4	0.1	-1.9	0.0
S_8	53.2 \pm 3.1	77.7 \pm 3.1	78.2 \pm 3.1	74.5 \pm 3.1	31.4 \pm 3.1
	56.4 \pm 2.5	77.2 \pm 2.5	73.1 \pm 1.9	72.6 \pm 2.5	28.8 \pm 2.3
	1.0	-0.2	-1.6	-0.6	-0.8

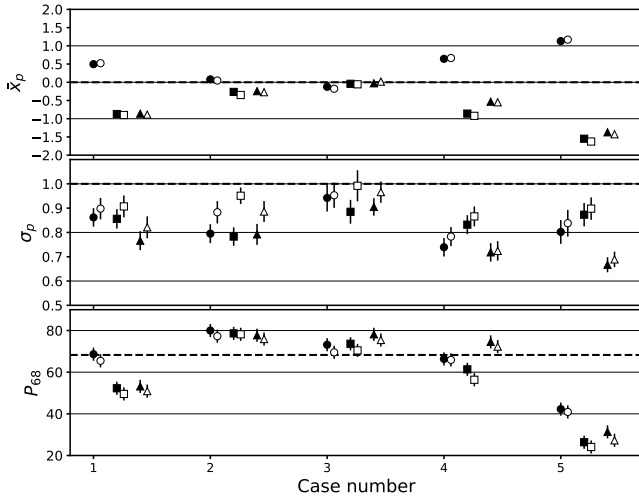


FIG. 8. Plots of the pull mean \bar{x}_p and rms σ_p and the 68.27% probability P_{68} . The circles, squares and triangles correspond to Ω_m , σ_8 and S_8 respectively. The solid markers correspond to KDE=1.5 and the open ones to KDE=1.0. The case numbers are the same as in Table IV or from left to right correspond to the top to bottom plots in Figure 7. For each case the markers have been displaced for clarity. The dashed lines give the expected values in the absence of biases.

As expected from our simple example in Section III A the results in this section clearly show that the poste-

riors confidence intervals can be substantially inflated. The question is, are there other sources that might contribute to the inflation of errors other than projection biases? Another source of error inflation is the Gaussian Kernel Density Estimator (KDE) algorithm [38] used by programs like Chainconsumer [37]. This program is widely used in weak lensing analysis to process the output of samplers like Multinest or Markov chain Monte Carlo programs. In the Gaussian KDE algorithm each point is replaced by a finite width Gaussian distribution. In Multinest the width of the Gaussian is controlled by a parameter called KDE.

Figure 8 shows the comparison of two analyses of all five ensemble tests using two different values of KDE in Multinest. The solid markers show the pull parameters \bar{x}_p and σ_p and the probability P_{68} for KDE=1.5. All these values come from the plots in Figure 7. The circles, squares and triangles correspond to Ω_m , σ_8 and S_8 and from left to right the Case number corresponds to the top to bottom plots in Figure 7. The open markers correspond to a reanalysis of all five ensemble tests using KDE=1.0. As expected a lower value of KDE produces narrower posterior and therefore smaller confidence intervals, which translates in larger values of σ_p and smaller values of P_{68} . For Cases 1, 4 and 5 the changes in σ_p are small and almost within error bars. The changes in σ_p are larger for Case 2, but this could be a fluctuation in the Gaussian fits to the pull distribution (the fits are unstable in this case) because the changes in the more stable P_{68} are the same for Case 2 than for all the other cases. So we see an improvement in the confidence intervals going from KDE=1.5 to the marginally low value of KDE=1.0, but it is not enough to account for the inflated values of the confidence intervals we observe in most of the ensemble tests.

In principle it is possible to go to low values of KDE but this requires increasing the number of points used to calculate posterior distributions. In samplers like Multinest this is controlled by the so called live-points. The live-points used in this paper (500) is the same that was used, for example, in the recently published DES Weak Lensing analysis using the first three years of data. This number of live-points typically produces about 5,000 points with weights large enough to contribute to the posterior distributions, but this number of points is not enough to produce smooth 95% confidence edges for two dimensional posteriors using KDE values of one or lower. Increasing the live-points by a factor of n (e.g. $n = 2, 4, 8, \dots$) increases the number of points in the posteriors by a factor of n but also increases the CPU time by the same n factor. The studies presented in this paper took about five months of running almost exclusively on 14 computer clusters with a total of 1728 CPUs, so it is not really an option to increase the CPU time by factors of two.

The ensemble test studies in this section clearly show that, 1) there could be strong biases in the peak of the posteriors, 2) that there is a strong possibility that the errors obtained from the posteriors are inflated and 3) that

there could be a strong bias in the number of times the true value falls inside the 68.27% confidence interval calculated using the posterior distributions. The question now is how will this change with an increase in statistics, or sky coverage, in weak lensing analysis. This is the subject of the following section.

IV. EXTRAPOLATING TO LARGER DATA SETS

In Section III we demonstrated that projection biases depend on where the true values of the parameters lie inside the prior's intervals. But we saw in Subsection III A that the projection biases also depend on how well the likelihood fits inside the ranges specified for the priors. If the likelihood fits well inside the prior's ranges then the projection biases essentially disappear. Then it is relevant to ask what will happen to the weak lensing analysis as the statistics, or the sky coverage and depth of the experiments increases. To give a first order answer to this question we simulated a factor of three and a factor of nine increase in statistics by reducing the two-point correlation covariance matrix by a factor of three and nine respectively. The factor of three increase in statistics intends to simulate the recent published results by DES using the data collected during the first three years of running as opposed to the first year analysis that we used in this paper. The factor of nine is an optimistic estimation of the increase in statistics for the final DES analysis with their six years of data taking. We have assumed that on top of the factor of six increase in statistics there will other improvements in the object reconstruction and the analysis that will produce an equivalent gain of a factor of nine increase in statistics.

Figures 9 shows the results of the projection biases in the peak of the posteriors when the two-point correlation matrix was divided by a factor of three, and Figure 10 when it was divided by a factor of nine. In both cases the studies were done using synthetic data vectors as in Section III B. An examination of Figures 5, 9 and 10 show that when the true values of n_s , Ω_b , h and $\Omega_\nu h^2$ are close to the middle of the priors range (center group of 27 points) the projection biases essentially disappear with the increase in statistics. When the true value of $\Omega_\nu h^2$ is close, or at, the minimum range (right group of 27 points) then with the increase in statistics the projection biases become more or less independent of the values of the other three parameters with biases being at or approaching the 1σ level. When the true value of $\Omega_\nu h^2$ is close the maximum range (left group of 27 points) then the pattern is more confusing, where the biases in Ω_m and σ_8 seem to become less dependent and the biases in S_8 seem to be more or less the same with an increase in statistics.

Studies using only cosmic shear, or 1x2pt analysis, and the ones using galaxy clustering and galaxy-galaxy lensing, or 2x2pt analysis, have less constraining power than

the analysis using all three two-point correlation functions, as the 3x2pt analysis used in this paper. Less constraining power means wider likelihoods which can translate into larger projection biases [40]. The same is true for weak lensing analysis in the w CDM framework. So even if the increase in statistics may soften the projection biases in 3x2pt analysis this paper shows that careful attention to projection biases is warranted even with the increase in statistics expected in future weak lensing analysis.

V. CONCLUSIONS

In the standard way of performing weak lensing analysis we should expect biases in the projected posterior distributions even when the analysis theory perfectly reflects Nature and there are no measurement errors. For example, for the DES Y3 WL analysis, and only one set of true parameters, these biases can be found in Reference [23]. In this paper we showed that these biases arise when two conditions are satisfied: 1) we are projecting, or marginalizing, over poorly constrained parameters that are correlated with the parameters that we want to measure, and 2) the true value of these poorly constrained parameters is displaced from the center of their prior intervals. In our case the poorly constrained parameters are h , n_s , Ω_b and Ω_ν , and the biased posterior distributions correspond to Ω_m , σ_8 and S_8 . Moreover we showed that, depending on how the poorly constrained parameters are correlated with the parameters we are interested in measuring, the projection biases can reinforce or weaken each others effects. For example, we showed that for the DES Y1 WL analysis the maximum reinforcement occurs when the true values of h and n_s are close to the top of the range of their priors and the true values of Ω_b and Ω_ν are close to the bottom of the range imposed by their priors. We also showed that the projection biases not only affect the shift of the posterior distribution but also their width, and that to first order we can assume that the larger the biases in the peak of the posteriors the more inflated the confidence intervals will be.

We could ask now the obvious question about how to correct these projection biases. Ideally one would include run by run corrections in the analysis procedure such that ensemble tests would produce an unbiased pull distribution [41]. In the absence of such a procedure the best we can do is to use a well informed guess for the true values of the poorly constrained parameters and apply average corrections as the ones studied in this paper. For example if we use the PDG [42] compilation for our true values, that is $h = 0.674$, $n_s = 0.965$ and $\Omega_b = 0.0493$ and for $\Omega_\nu h^2$ we use the minimum allowed by neutrino oscillation experiments, which corresponds to (34,48,48,1.2) per cent of their ranges respectively, then we see that we should apply the corrections for the case listed in the first row of Table IV. This case corresponds to the rightmost square symbol in Figure 5 and to the first row

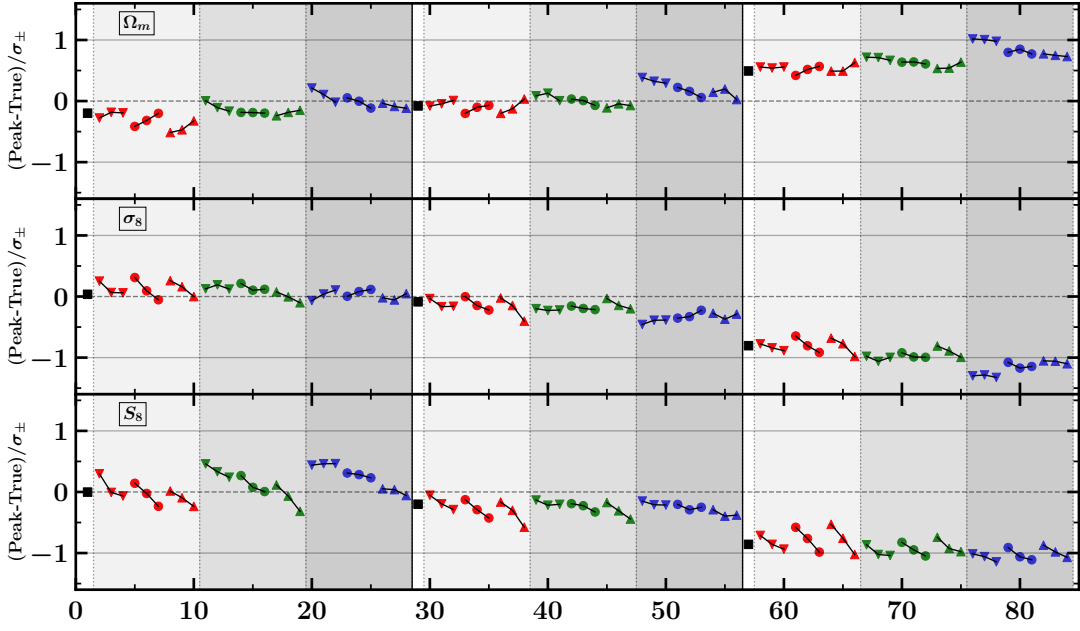


FIG. 9. Same set of plots as shown in Figure 5 but for an analysis reducing the covariance matrix of the fit to the three two-point correlation functions by a factor of three. The factor of three was selected to simulate the recently released DES Y3 Weak Lensing analysis.

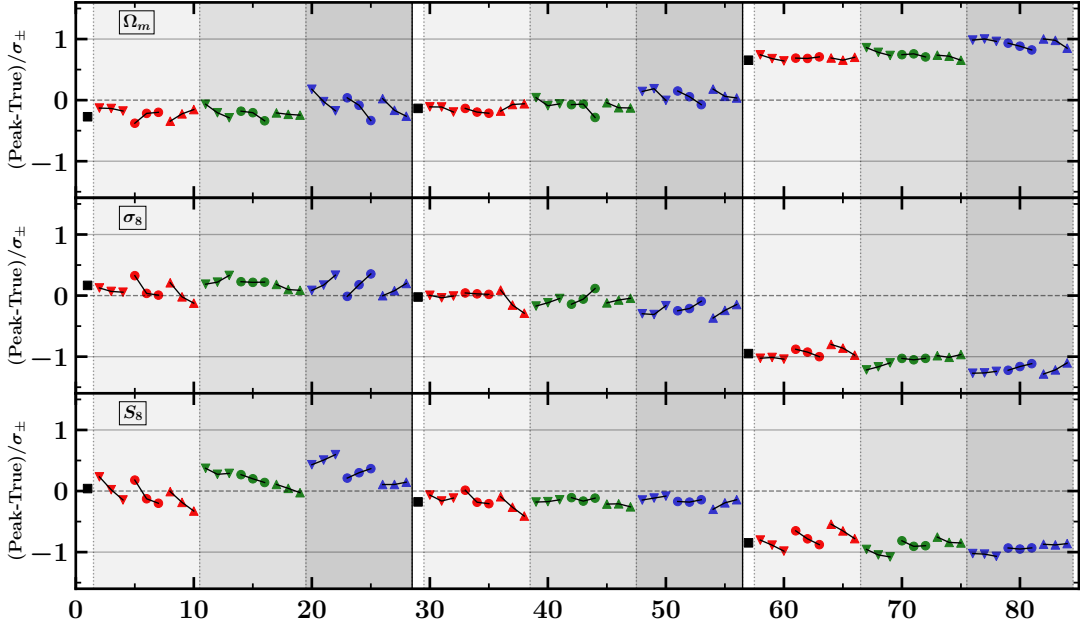


FIG. 10. Same set of plots as shown in Figure 5 but for an analysis reducing the covariance matrix of the fit to the three two-point correlation functions by a factor of nine. The factor of nine was selected to simulate an optimistic increase in the statistics of the full analysis of the six years of DES data.

of plots in Figure 7. Then the corrections for the central values of $(\Omega_m, \sigma_8, S_8)$ are $(-0.45\sigma_-, 0.78\sigma_+, 0.82\sigma_+)$ and the multiplicative factors for correcting the errors are $(0.86, 0.86, 0.77)$. These corrections apply to the values

in row four of Table II, and the corrected values are

$$\Omega_m = 0.260^{+0.028}_{-0.023}, \quad \sigma_8 = 0.856^{+0.051}_{-0.048}, \quad S_8 = 0.798^{+0.020}_{-0.018}$$

Even though we have only estimated the corrections for the analysis of three years of DES data, a comparison of Figures 5 and 9 for the case described above indicate that

these correction probably will not change much between the Y1 and Y3 weak lensing analysis. So for the central values we can apply the corrections derived from the rightmost squares in Figure 9 and for the errors the corrections derived from the top row pull plots in Figure 7. Then the corrections for the central values of the posteriors will be $(-0.49\sigma_-, 0.81\sigma_+, 0.86\sigma_+)$ and the correction factors for the errors will be the same as in the previous case $(0.86, 0.86, 0.77)$. Applying these corrections to the recently published DES Y3 WL results (see Table II and Figure 7 in Reference [9]) we get

$$\Omega_m = 0.324^{+0.028}_{-0.027}, \quad \sigma_8 = 0.764^{+0.034}_{-0.042}, \quad S_8 = 0.791^{+0.013}_{-0.013}$$

These corrections produce smaller error bars and bring the new DES Λ CDM results to be in complete agreement with the Planck results. We should note that the reduction in the size of the error bars coming from the pull tests is not negligible. For example the largest reduction in σ going from DES Y1 to Y3 is a factor of 0.74 for S_8 . While from the pull tests for S_8 we get a reduction in σ of 0.77 ± 0.04 for $\sum m_\nu = 0.06$ eV and 0.79 ± 0.04 for $\sum m_\nu = 0.42$ eV (see the two top rightmost plots in Figure 7). The current PDG limit for the sum of the neutrino masses is $\sum m_\nu < 0.12$ eV

As we saw, for example in Section III A, the projection biases disappear if the likelihood distribution is very well contained inside all of the allowed intervals specified by the priors. This may lead one to believe that given the large increase in statistics of future experiments projection biases will cease to be a problem in the future. But this is unlikely to happen because the tightening of the priors in poorly constrained parameters reduces the errors in the parameters that we are interested in measuring. Therefore there will always be a push for tightening priors and most likely all future weak lensing experiment will have to consider paying close attention to the behaviour of their projection biases.

ACKNOWLEDGMENTS

We would like to thank Joe Zuntz and Marc Paterno for useful exchanges about CosmoSIS and Alex Drlica-Wagner and Francisco Javier Sanchez for carefully reading the manuscript and providing many useful comments. Prudhvi Chintalapati would like to thank the Visiting Scholar Award Program of the Universities Research Association for providing the funding to visit Fermilab and be an integral part of the studies presented in this paper, and also thank Dr. Swapan Chattopadhyay of Northern Illinois University for his financial support. This manuscript has been authored by Fermi Research Alliance, LLC under Contract No. DE-AC02-07CH11359 with the U.S. Department of Energy, Office of High Energy Physics.

Appendix A: Minimum Credible Intervals

Given a normalized posterior $P(x)$ we want to calculate two limits A and B such that

$$\int_A^B P(x) dx = a_{68} \quad (\text{A1})$$

where $a_{68} = \text{erf}(1/\sqrt{2}) \approx 0.6827$. Equation A1 is not enough to determine the values of A and B , another condition is needed. Here we will impose the condition that the interval $B - A$ be minimal. Then the problem we want to solve is the minimization of the interval $B - A$ subject to condition A1. Using a Lagrange multiplier we need to minimize

$$Q = B - A + \lambda \left(\int_A^B P(x) dx - a_{68} \right) \quad (\text{A2})$$

Given the minimization conditions

$$\frac{\partial Q}{\partial B} = \frac{\partial Q}{\partial A} = \frac{\partial Q}{\partial \lambda} = 0 \quad (\text{A3})$$

we obtain

$$1 + \lambda P(B) = 0, \quad \text{and} \quad -1 - \lambda P(A) = 0 \quad (\text{A4})$$

plus Equation A1, which leads to the relation

$$P(A) = P(B) \quad (\text{A5})$$

If $P(x)$ has only one peak then the previous condition also ensures that the peak is contained in the credible interval. This happens because $P(x)$ steadily falls on both sides of the peak. If $P(x)$ has more than one peak then both peaks could be inside of the credible interval, or condition A5 could give rise to two credible intervals and one would select the smaller of the two.

Appendix B: Calculating P_{68} From Pull Parameters

The left plot in Figure 11 shows a conceptual posterior distribution for one experiment together with the peak of the distribution x_p and the true value x_T . The true value lies inside the 68.27% confidence interval if the condition $x_p - \sigma_- \leq x_T \leq x_p + \sigma_+$ is satisfied, which translates into the inequalities

$$-\sigma_+ \leq x_p - x_T \leq \sigma_- \quad (\text{B1})$$

For a very large number of experiment we can form the pull defined as in Equation 19. When x_T is close to σ_- we have to divide $x_p - x_T$ by σ_- and the right inequality in Equation B1 becomes $\text{pull} \leq 1$, and when x_T is close to σ_+ the left inequality in the same equation becomes $\text{pull} \geq -1$. Therefore for a large number of experiments the condition for finding the true value inside the 68.27%

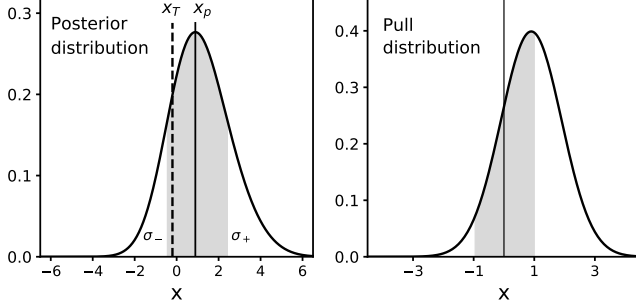


FIG. 11. Conceptual posterior distribution for a single experiment (left) and pull distribution (right). For a large number of experiments the 68.27% area under the posteriors translates into the $[-1, 1]$ area under the pull distribution.

area of the posterior translates into $-1 \leq \text{pull} \leq 1$, as illustrated in the right plot of Figure 11. Then for a Gaussian pull the probability of finding the true value inside the 68.27% area of the posterior is given by

$$P_{68} = \frac{1}{\sqrt{2\pi}\sigma_p} \int_{-1}^1 dx e^{-\frac{1}{2}\left(\frac{x-\bar{x}_p}{\sigma_p}\right)^2} \quad (\text{B2})$$

$$= \frac{1}{2} \left\{ \text{erf}\left(\frac{1-\bar{x}_p}{\sqrt{2}\sigma_p}\right) + \text{erf}\left(\frac{1+\bar{x}_p}{\sqrt{2}\sigma_p}\right) \right\} \quad (\text{B3})$$

where \bar{x}_p and σ_p are the mean and rms of the pull distribution and we have used the property $\text{erf}(-x) = -\text{erf}(x)$. The error in P_{68} is calculated in the standard way

$$\sigma_{P_{68}} = \sqrt{\left(\frac{\partial P_{68}}{\partial \bar{x}_p} \Delta \bar{x}_p\right)^2 + \left(\frac{\partial P_{68}}{\partial \sigma_p} \Delta \sigma_p\right)^2} \quad (\text{B4})$$

-
- [1] P. Fisher *et al.* (SDSS), *The Astronomical Journal* **120**, 1198 (2000).
 - [2] D. M. Wittman, J. A. Tyson, D. Kirkman, I. Dell’Antonio, and G. Bernstein, *Nature* **405**, 143 (2000).
 - [3] D. J. Bacon, A. R. Refregier, and R. S. Ellis, *MNRAS* **318**, 625 (2000).
 - [4] L. van Waerbeke *et al.* (CFHT), *A&A* **358**, 30 (2000).
 - [5] A. Amon *et al.* (DES), arXiv:2105.13543 (2021).
 - [6] L. F. Secco *et al.* (DES), arXiv:2105.13544 (2021).
 - [7] S. Pandey *et al.* (DES), arXiv:2105.13545 (2021).
 - [8] A. Porredon *et al.* (DES), arXiv:2105.13546 (2021).
 - [9] T. M. C. Abbott *et al.* (DES), arXiv:2105.13549 (2021).
 - [10] T. Hamana *et al.* (HSC), *PASJ* **72**, 16 (2020).
 - [11] M. Asgari *et al.* (KiDS), *A&A* **645**, A104 (2021).
 - [12] C. Heymans *et al.* (KiDS), *A&A* **646**, A140 (2021).
 - [13] T. Tröster *et al.* (KiDS), *A&A* **649**, A88 (2021).
 - [14] X. Li *et al.* (HSC), arXiv:2107.00136v1 (2021).
 - [15] Euclid: <https://www.euclid-ec.org>.
 - [16] LSST: <https://www.lsst.org>.
 - [17] NRST: <https://roman.gsfc.nasa.gov>.
 - [18] J. DeRose *et al.* (DES), arXiv:2105.13547 (2021).
 - [19] H. Hildebrandt *et al.* (KiDS), *MNRAS* **465**, 1454 (2017).
 - [20] B. Joachimi *et al.* (KiDS), *A&A* **646**, A129 (2021).
 - [21] E. Krause *et al.*, arXiv:1706.09359v1 (2017).
 - [22] The studies presented in this paper required about six million hours of CPU time, 83% of which was used in the ensemble tests.
 - [23] E. Krause *et al.* (DES), arXiv:2105.13548 (2021).
 - [24] T. M. C. Abbott *et al.* (DES), *Phys. Rev. D* **98**, 043526 (2018).
 - [25] J. Zuntz, M. Paterno, E. Jennings, D. Rudd, A. Manzotti, S. Dodelson, S. Bridle, S. Sehrish, and J. Kowalkowski, *Astronomy and Computing* **12**, 45 (2015).
 - [26] To run CosmoSIS use the installer available at <https://bitbucket.org/joezuntz/cosmosis/wiki/Home>. ()
 - [27] C. M. Hirata and U. Seljak, *Phys. Rev. D* **70**, 063526 (2004).
 - [28] C. M. Hirata and U. Seljak, *Phys. Rev. D* **82**, 049901(E) (2010).
 - [29] S. Bridle and L. King, *New Journal of Physics* **9**, 444 (2007).
 - [30] M. A. Troxel *et al.*, *Phys. Rev. D* **98**, 043528 (2018).
 - [31] A. Lewis, A. Challinor, and A. Lasenby, *The Astrophysical Journal* **538**, 473 (2000).
 - [32] R. E. Smith, J. A. Peacock, S. D. M. W. A. Jenkins, C. S. Frenk, F. R. Pearce, P. A. Thomas, G. Efstathiou, and H. M. P. Couchman, *Mon. Not. R. Astron. Soc.* **341**, 1311 (2003).
 - [33] S. Bird, M. Viel, and M. G. Haehnelt, *Mon. Not. R. Astron. Soc.* **420**, 2551 (2012).
 - [34] R. Takahashi, M. Sato, T. Nishimichi, A. Taruya, and M. Oguri, *The Astrophysical Journal* **761**, 152 (2012).
 - [35] (), used CosmoSIS version v1.6, dated 2019-07-09, which can be found as branch v1.6 in <https://bitbucket.org/joezuntz/cosmosis/commits/bed016fb4ea69187a072db1fb4f2ea3d57a57f76>.
 - [36] F. Feroz, M. P. Hobson, and M. Bridges, *Mon. Not. R. Astron. Soc.* **398**, 1601 (2009).
 - [37] S. R. Hinton, ChainConsumer, *The Journal of Open Source Software* **1**, 00045 (2016), (See also <https://samreay.github.io/ChainConsumer/>).
 - [38] See for example https://en.wikipedia.org/wiki/Kernel_density_estimation.
 - [39] W. T. Eadie, D. Drijard, F. James, M. Roos, and B. Sadoulet, *Statistical Methods in Experimental Physics* (North Holland, 1971) Chap. xx, pp. 277–278.
 - [40] These studies are currently under way.
 - [41] We are working on that but have not completely solve the problem yet.
 - [42] Particle Data Group: <https://pdg.lbl.gov>.